Biophysical Journal
Article

Biophysical Society

Effect of RNA on the supramolecular architecture of α-synuclein fibrils

Antonia Intze,[1,2,3,*] Maria Eleonora Temperini,[1,3] Jakob Rupert,[4,5,6] Raffaella Polito,[3,7] Alexander Veber,[8,9] Ljiljana Puskar,[8] Ulrich Schade,[8] Michele Ortolani,[3] Elsa Zacco,[5] Gian Gaetano Tartaglia,[5,10] and Valeria Giliberti[1,*]

[1]Center for Life Nano- & Neuro-science, Istituto Italiano di Tecnologia (IIT), Rome, Italy; [2]Department of Biochemical Sciences "Alessandro Rossi Fanelli", Sapienza University of Rome, Rome, Italy; [3]Department of Physics, Sapienza University of Rome, Rome, Italy; [4]Department of Biology and Biotechnologies "Charles Darwin", Sapienza University of Rome, Rome, Italy; [5]Centre for Human Technologies (CHT), Istituto Italiano di Tecnologia (IIT), Genova, Italy; [6]Molecular Neuroscience, German Center for Neurodegenerative Diseases (DZNE), Bonn, Germany; [7]Institute for Photonics and Nanotechnologies IFN-CNR, Rome, Italy; [8]Institute for Electronic Structure Dynamics, Helmholtz-Zentrum Berlin für Materialien und Energie GmbH, Berlin, Germany; [9]Department of Chemistry, Humboldt-Universität zu Berlin, Berlin, Germany; and [10]Catalan Institution for Research and Advanced Studies, ICREA, Barcelona, Spain

ABSTRACT Structural changes associated with protein aggregation are challenging to study, requiring the combination of experimental techniques providing insights at the molecular level across diverse scales, ranging from nanometers to microns. Understanding these changes is even more complex when aggregation occurs in the presence of molecular cofactors such as nucleic acids and when the resulting aggregates are highly polymorphic. Infrared (IR) spectroscopy is a powerful tool for studying protein aggregates since it combines the label-free sensitivity to the cross-β architecture, an inherent feature of protein supramolecular aggregates, with the possibility to reach nanoscale sensitivity by leveraging atomic force microscopy (AFM)-assisted detection. Here, we present a combined approach that detects IR spectral markers of aggregation using various IR spectroscopy techniques, covering micro-to-nanoscale ranges, to study the effect of RNA on the supramolecular architecture of α-synuclein amyloid aggregates. We show a clear impact of RNA consistent with enhanced intermolecular forces, likely via a stronger hydrogen-bonded network stabilizing the cross-β architecture. AFM-assisted IR spectroscopy was crucial to assess that the more ordered the aggregates are, the stronger the structural impact of RNA. In addition, an RNA-induced reduction of the degree of polymorphism within the aggregate population is obtained.

SIGNIFICANCE The advances in the study of protein aggregation have highlighted the importance of non-proteic cofactors in the process, with nucleic acids being among the most prominent. In the following work, we show the effect of RNA on the supramolecular architecture of α-synuclein (αS) fibrils during the in vitro protein aggregation process. This presents an important step in the understanding of αS pathological mechanisms, as well as the potential development of RNA-based therapeutics and diagnostics for neurodegenerative processes, involving αS. We also provide a widely applicable multiscale method that combines various infrared spectroscopy techniques, covering micro-to-nanoscale ranges, for the study of structural changes associated with protein aggregation processes.

INTRODUCTION

The interaction of aggregation-prone proteins with other biological molecules can significantly affect the protein aggregation pathway, potentially leading to various aggregate polymorphs and different disease outcomes in pathological conditions (1). Understanding the relationship between aggregate morphology and molecular structure is essential for shedding light on the diverse protein self-assembly processes. In this context, we investigate how the aggregation of α-synuclein (αS) is affected when coaggregated in vitro with RNA. αS is a protein found in the presynaptic region of the human brain (2,3) that has been linked to Parkinson's disease (4–6), and it belongs to the class of intrinsically disordered proteins (IDPs). IDPs do not exhibit a single conformation in their monomeric state, but rather a

Submitted December 19, 2024, and accepted for publication April 29, 2025.

*Correspondence: antonia.intze@uniroma1.it or valeria.giliberti@iit.it

Antonia Intze, Maria Eleonora Temperini, and Jakob Rupert contributed equally to this work.

Editor: Samrat Mukhopadhyay.

https://doi.org/10.1016/j.bpj.2025.04.031

multitude of energy-equivalent conformations (7,8). Such a feature is known to result in a high degree of polymorphism of the aggregates resulting from the self-assembly process of the IDPs (26). A wealth of in vitro aggregation studies has extensively investigated the phase transition of αS from protein monomers to stable aggregate chains, known as amyloid fibrils (9–11), also monitoring how the structural heterogeneity (polymorphism) can be altered by various aggregation conditions (7,12–23). Recently, it has been shown that when αS is coincubated in vitro with RNA, the kinetics of αS self-assembly aggregation is affected (24). Specifically, RNA exacerbates the aggregation propensity of αS, with a more pronounced effect for the C-terminal isoform truncated at position N103 (αS_{103}), which has been linked to a worse disease outcome and increased aggregation of endogenous αS in patients (25). The impact on aggregation kinetics was computationally and experimentally linked to the fact that αS gains the ability to sequester RNA molecules once it is in the form of aggregates. The same study has also suggested that such sequestration of RNA not only has an impact on the aggregation kinetics, but also on the structural characteristics of αS aggregates. However, no experimental evidence has been provided so far.

In the search to monitor possible structural effects of RNA on αS aggregates, the structural heterogeneity poses challenges when using volume-averaging techniques since there might be a different propensity of aggregates to interact with RNA, depending on their structure (27). Protein concentration, ionic strength (28), and coincubation with non-protein cofactors (29) were all identified as factors affecting the degree of polymorphism of αS aggregates. In addition, several studies conducted on other aggregation-prone proteins have revealed that the presence of nucleic acids can alter not only the protein aggregation kinetics (30), but also the fibril architecture (31,32). At the same time, high-resolution structural techniques, such as cryogenic electron microscopy (31) and solid-state nuclear magnetic resonance (33), cannot provide a complete structural picture that captures the full breadth of heterogeneity. In this framework, optical vibrational spectroscopies represent a powerful tool (34–39). In particular, infrared (IR) vibrational spectroscopy emerges as an important experimental strategy since it combines two main advantages. On the one hand, it provides a great label-free sensitivity to the cross-β architecture inherently linked to the protein fibril supramolecular architecture. This offers a great advantage over other optical spectroscopies used to study protein aggregation and particularly suited for kinetic studies. Indeed, fluorescent probes, e.g., thioflavin T, activate when the cross-β architecture is formed (40) and circular dichroism (CD) features high sensitivity to aggregate formation but low specificity to the details of supramolecular protein architecture. Moreover, IR allows for a diversity of approaches, from microspectroscopy techniques working at the macroscale down to ultrasensitive techniques at the nanoscale, all relying on the same light-matter interaction process of vibrational absorption. This latter feature facilitates the integration and benchmarking of results obtained with microspectroscopy and nanospectroscopy approaches from samples of the same protein under the same aggregation conditions, something that, again, would not be possible with fluorescence and CD spectroscopies or high-resolution structural techniques.

Here, we present a toolset for studying the structural effects of RNA on αS amyloid fibrils with diverse degrees of polymorphism. We employ Fourier transform IR (FTIR) spectroscopy in the form of microspectroscopy (micro-FTIR) together with IR nanospectroscopy approaches relying on the use of an atomic force microscopy (AFM), both in the form of scattering-type scanning near-field optical microscopy (s-SNOM) and photothermal-expansion IR nanospectroscopy (AFM-IR). Spectroscopic analysis is also corroborated by pure AFM for morphological characterization of the fibrils. We observe a clear effect of RNA on the supramolecular architecture of αS fibrils, with an enhancing of the intermolecular forces, likely within the hydrogen-bonded (H-bond) network of β-sheets characteristic of the cross-β fibril structure. The application of IR nanospectroscopy, which correlates morphological to spectroscopic information, is crucial to assess that the effect of RNA also depends on the degree of order of aggregates. We clearly observe in the high polymorphic αS_{103} isoform that the more ordered the aggregates appear, such as amyloid fibrils, the stronger the structural impact of RNA on their supramolecular architecture. Such structural effect is accompanied by an RNA-induced reduction of the structural heterogeneity within the mature aggregate population.

MATERIALS AND METHODS

Protein purification

The protein was purified according to existing protocols (24). Briefly, competent *E. coli* BL21 [DE3] cells (Thermo Fisher Scientific, Waltham, MA) expressing αS_{WT} were lysed at 95°C and the protein was isolated via a two-step precipitation protocol with streptomycin sulfate and ammonium sulfate. After dialysis, the protein was further purified with subsequent ion-exchange and size-exclusion chromatography steps. The purified protein was immediately pooled, aliquoted, and kept at −80°C. Concentration was checked with a bicinchoninic acid assay and purity via spectropolarimetry and sodium dodecyl sulfate-polyacrylamide gel electrophoresis.

Preparation of αS fibrils

Purified αS_{WT} and αS_{103} samples were quickly defrosted and immediately filtered with a 0.22 μm syringe filter (Merck Millipore, Burlington, MA). Total yeast RNA (Roche, Basel, Switzerland) was resuspended in aggregation buffer (20 mM potassium phosphate [pH 7.2], 100 mM KCl, 5 mM $MgCl_2$) to form a stock solution with a concentration of 5 mg mL^{-1}. Protein and RNA were mixed immediately before the start of the assay to the final concentrations of 50 μM and 0.5 mg mL^{-1}, respectively, with the addition of 0.05% NaN_3. Aggregation assays were performed in a Thermomixer

C device (Eppendorf, Hamburg, Germany) in DNA LoBind 1.5 mL tubes (Eppendorf) at 37°C with constant agitation at 800 rpm for 144 and 5.5 h for αS_{WT} and αS_{103}, respectively.

Seeded aggregation of αS_{WT}

αS_{WT} aggregates in the presence and absence of RNA were prepared as described above. Samples were centrifuged at 17,000 × *g* for 1 h at room temperature and the supernatant was removed. The pelleted fibrils were resuspended in sterile 1× phosphate buffered saline (PBS) and RNase A (ThermoFisher Scientific) was added to degrade leftover RNA. The RNA digestion was performed for 30 min at 37°C and stopped with the addition of RiboLock RNase inhibitor (ThermoFisher Scientific) directly into the suspension. The sample was again centrifuged at 17,000 × *g* for 1 h at room temperature, the supernatant removed and the pellet washed with PBS. This was repeated a further two times to avoid any potential RNA or RNase A contamination. In the end, the pelleted fibrils were resuspended in 1× PBS, aliquoted in Protein LoBind tubes (Eppendorf) and kept at −80°C until use. The seeds were sonicated at room temperature for 10 min immediately before the experiment.

Protein aggregation assays

The protein aggregation assays were performed as described previously (24). Briefly, the protein aliquots were kept at −80°C, thawed in cold water, and immediately filtered through a 0.22 μm syringe filter (Merck Millipore). Total yeast RNA (Roche) was prepared as described above. Proteostat™ (Enzo Life Science, Farmingdale, NY) was used as the amyloid reporter dye at 1000× dilution as per the manufacturer's instructions. The experiment was conducted in a 96-well plate with a protein low-binding surface (Grenier Bio-One, Kremsmünster, Austria) using a 3 mm borosilicate glass bead in a Tecan Spark instrument (Tecan Group, Männedorf, Switzerland). The excitation wavelength was set to 505 nm and the emission to 590 nm. Plates were incubated at 37°C with constant double-orbital shaking at 200 rpm. Reads were taken every 5 min for αS_{103} over 6 h and every 10 min for αS_{WT} over 24 h, with each read represented as an average of 10 scans.

CD

The protein was quickly thawed and the buffer was immediately exchanged for the CD buffer containing 20 mM potassium phosphate (pH 7.2), 100 mM KF, and 5 mM MgF_2 on a PD-10 desalting column (Cytiva Life Sciences, Marlborough, MA). Total yeast RNA (Roche) was resuspended in CD buffer and the aggregation samples were prepared as described above. At identical time points, 150 μL of the sample was transferred to a 1 mm Quartz cuvette (Hellma, Müllheim, Germany), and the measurements were taken at 37°C with a Jasco J-1500 instrument (JASCO, Tokyo, Japan). Spectra were recorded between 190 and 320 nm with a scanning speed of 100 nm min^{-1} at a bandwidth of 1 nm. The final spectrum represents an average of 10 scans. The spectra of RNA alone were subtracted from the spectra of the protein-RNA coaggregation sample and compared with the protein-only.

FTIR microspectroscopy

For the micro-FTIR experiments, 20 μL of the sample was deposited at the center of the top surface of 1-mm-thick CaF_2 windows and let to dry completely under a gentle nitrogen flow in low-humidity conditions. The micro-FTIR experiments presented in this work were performed using three experimental setups probing different sampling areas. Micro-FTIR spectra reported in Fig. 1 *F* were acquired with an IFS 66v/S spectrometer combined with a gas-purged Hyperion IR-microscope (Bruker Optics, Ettlingen, Germany). The Hyperion microscope was equipped with a 15× Cassegrain objective lens (numerical aperture [NA] = 0.4) and a liquid-nitrogen-cooled mercury-cadmium-telluride (MCT) detector. The knife-edge aperture used for the experiments was 200 × 200 μm^2. Spectra were recorded in transmission mode within the spectral range 800–6000 cm^{-1} with a resolution of 2 cm^{-1} and 512 scans. Micro-FTIR spectra reported in Fig. 2 *A* were acquired using a Vertex 80 spectrometer (Bruker Optics) combined with a Hyperion 3000 IR-microscope (Bruker Optics) at the IRIS beamline at BESSY II of the Helmholtz Zentrum Berlin. The Hyperion 3000 microscope was purged continuously with gaseous nitrogen and was equipped with a 15× Cassegrain objective lens (NA = 0.4). The data of Figs. 2, *A*, *C*, *D* and 3, *A* and *B* were acquired with a liquid nitrogen-cooled MCT detector using a knife-edge aperture of 15 × 15 μm^2, while the data of Fig. 2 *E* with a liquid-nitrogen cooled 64 × 64 pixel focal plane array (FPA) detector covering a total area of 173 × 173 μm^2 (single pixel area is 2.7 × 2.7 μm^2). Spectra were recorded using the internal Globar source in transmission mode within the spectral range 800–4000 cm^{-1} with a resolution of 2 cm^{-1} and 128 (64) scans for the MCT (FPA) detector.

AFM-IR nanospectroscopy

Three aliquots of 2 μL were drop-cast onto the 1 × 1 cm template-stripped gold surfaces (Platypus Technologies, Madison, WI, 0.3 nm nominal roughness) for 5 min, then rinsed with 40 μL Milli-Q water to achieve a sparse area of deposited protein aggregates and let dry for 1 h under a gentle nitrogen flow in a controlled low-humidity environment. AFM topographies and AFM-IR spectra were measured using the nanoIR2 platform (Anasys Instruments, Santa Barbara, CA) equipped with a quantum cascade laser operating between 900 and 1900 cm^{-1} (MIRcat-xB, Daylight Solutions, San Diego, CA). The probes were gold-coated silicon cantilevers with an elastic constant of 0.07–0.4 N m^{-1} and a nominal radius of 25 nm (PR-EX-nIR2-10, provided by Anasys Instruments). All measurements were done in contact mode and at room temperature.

Topography

Image data were acquired at a line rate of 1–1.5 Hz and a resolution of 20 nm per pixel. The AFM images were flattened using the built-in Analysis Studio software (Anasys Instruments). The persistence length was calculated from the contour length (C) and the end-to-end distance (E) of the fibrils by fitting E^2 as a function of C (Fig. S5). These measurements were conducted on single αS_{WT} and αS_{WT+RNA} fibrils at the edges of bundles, sometimes intersecting each other.

Spectra

The AFM-IR spectra were collected within the range 1415–1900 cm^{-1} at 2 cm^{-1} spectral resolution and 256 coaverages. Spectra were averaged from at least 12 measurements.

Scattering-type scanning near-field optical microscopy

The $\alpha S_{WT,seed}$ fibrils were dropcast on ultraflat gold surfaces as described for the AFM-IR measurements. The s-SNOM measurements of individual $\alpha S_{WT,seed}$ agglomerate fibril bundles were performed with a neaSNOM system (attocube systems, Haar, Germany) coupled to the broadband synchrotron source at the IRIS beamline at BESSY II of the Helmholtz Zentrum Berlin with a spectral resolution of 6 cm^{-1}. The s-SNOM measurements of the $\alpha S_{WT,seed}$ and $\alpha S_{WT+RNA,seed}$ were done in tapping mode using an Arrow-NCPt Pt/Ir-coated AFM probe (tip radius <25 nm, NanoWorld, Neuchâtel, Switzerland) and a PPP-NCSTAu Au-coated AFM probe (tip radius <50 nm, Nanosensors, Neuchâtel, Switzerland), respectively.

Data analysis

The IR spectra shown in Fig. 1 were baseline corrected, smoothed with a spline algorithm, and normalized by IgorPro software (version 6.22A, Wavemetrics, Lake Oswego, OR). To determine the relative amount of secondary structure components, the amide-I and -II bands were fitted in the 1500–1700 cm^{-1} spectral range using eight Lorentzian components. Second-order derivatives of the IR spectra determined the number and peak positions of the Lorentzian line shapes. The amide-II band was fitted with three components centered at 1523, 1552, and 1590 cm^{-1} with intensity as the free parameter and full width at half maximum (FWHM) fixed to 40, 60, and 40 cm^{-1}, respectively. The amide-I band was deconvolved using five Lorentzian components centered at 1625, 1640, 1652, 1670, and 1690 cm^{-1} ranging $\pm$ 2 cm^{-1}, with a fixed FWHM equal to 25 cm^{-1} and intensity as the free parameter. The Lorentzian line shapes used to deconvolve the amide-I band are assigned to different secondary structure components of the protein: 1623–1627 cm^{-1} is ascribed to antiparallel and parallel β-sheet, 1638–1642 cm^{-1} to disordered, 1650–1654 cm^{-1} to α-helix, 1668–1672 cm^{-1} to turn, and 1688–1692 cm^{-1} to antiparallel β-sheet (41).

The ω_β analysis in the single MCT spectra shown in Figs. 2 *C* and 3 *A*, was done using OPUS software (version 8.7, Bruker Optics). The second-order derivatives of the IR spectra were first calculated by applying the Savitzky-Golay algorithm (nine smoothing points). Then, the minima of the second-order derivatives in the 1624–1632 cm^{-1} range were identified using the *peak picking* command of OPUS. After baseline correction and normalization at the amide-I and -II area, the same spectra were analyzed with principal component analysis (PCA) in the 1605–1640 cm^{-1} range (Figs. 2, *D*, *E* and 3 *B*) using Quasar 1.9.2 software package (42).

The 64 × 64 IR spectra acquired with the FPA detector were baseline corrected in the range 1480–1730 cm^{-1} and integrated in the 1490–1720 cm^{-1} range to obtain a map of the amide-I and -II absorbance intensity. To obtain the map of the ω_β, the second-order derivatives were calculated as described for the single MCT spectra. Spectra with no or two second-order derivative minima in the 1624–1632 cm^{-1} range, corresponding to spectra with a low signal-to-noise ratio (SNR), were not considered for the analysis of the ω_β. For a further exclusion of the pixels with a low protein content, a mask was applied to the amide-I and -II absorbance intensity map selecting the pixels with a value in the 50–100% range with respect to the maximum using Gwyddion software (version 2.61). The same mask was applied to the ω_β map. After normalization at the amide-I and -II area, the spectra corresponding to the selected pixels were analyzed with PCA in the 1605–1640 cm^{-1} (Fig. 2 *E*) by the Quasar 1.9.2 software.

FTIR and fluorescence data in Fig. 1, *B* and *D* were fitted using the Hill function. Parameters for the best fitting curves of the αS_{103} ($\alpha S_{103+RNA}$) FTIR data are: A = 0.81 $\pm$ 0.03 (0.77 $\pm$ 0.05), c = 5.9 $\pm$ 1.5 (19 $\pm$ 10), k = 1.6 $\pm$ 0.1 h (2.9 $\pm$ 0.1 h). Parameters for the best fitting curves of the αS_{103} ($\alpha S_{103+RNA}$) time-resolved fluorescence data are: A = 0.91 $\pm$ 0.02 (1.02 $\pm$ 0.02), c = 11.6 $\pm$ 0.9 (4.8 $\pm$ 0.3), k = 3.62 $\pm$ 0.03 h (1.19 $\pm$ 0.02 h).

RESULTS

Initial focus: The impact of RNA on de novo αS aggregation kinetics and fibril morphology

Sample preparation for all IR experiments, from micro- to nanospectroscopy, consisted of promoting the de novo aggregation in solution and depositing droplets of the sample on solid substrates at a given time *t*. The samples were dried to "freeze" the protein at specific aggregation stages. This procedure allowed us to perform various measurements on fibrils grown under the same experimental conditions and provided a better benchmark between micro-FTIR and IR nanospectroscopy approaches. Although efforts are being made to overcome the limitation of performing AFM-based IR nanospectroscopy in liquid (43–46), working with dried samples remains the standard when a high SNR is required, as in this application. As a first step, we verified that the structural information obtained through IR spectroscopy of deposited and dried aggregates reflects the protein state formed during in vitro aggregation in solution. To achieve this, we benchmarked IR data against time-resolved Proteostat™ fluorescence spectroscopy and CD, both performed on proteins in liquid suspension. Proteostat™ is used as a marker of aggregation through the direct binding to the cross-β architectures, resulting in an increase in fluorescence upon amyloid formation. The formation of extended β-sheets featuring strong intermolecular interactions, where the β-strands are oriented perpendicular to the fibril axis, creates the hallmark cross-β architecture of amyloid fibrils (47,48). To assist the reader, we provide a simplified sketch of a representative protein fibril with a parallel cross-β arrangement, highlighting the H-bonds between the β-strands that stabilize the fibril (Fig. 1 *A*). For the characterization of αS aggregation by IR spectroscopy, we focused on the amide-I band (1610–1690 cm^{-1}), which arises from the coupled C=O stretching vibrational modes along the protein backbone. As such, it is the primary IR band sensitive to protein secondary structure as well as to the characteristic supramolecular cross-β architecture of protein fibrils (49–52). In Fig. 1 *B*, we report representative amide-I FTIR spectra and their individual components obtained from amide-I deconvolution, one acquired when αS_{WT} is in the oligomeric state at the beginning of the aggregation process (*bottom*), and another obtained at the end of the process when mature fibrils have formed (*top*). The latter spectrum shows a visible increase in the antiparallel and parallel β-sheet peak $(\beta\text{-sheet})_{P,AP}$, a spectral marker of fibrils and aggregates in general, thus indicating their formation with respect to the less β-structure-rich oligomers. The characteristic cross-β architecture of fibrils can involve either a parallel or antiparallel arrangement of intermolecular β-sheets, both resulting in an intense absorption peak centered at frequencies (1620–1630 cm^{-1}) slightly lower than those of native β-sheets (53,54). As confirmed by the deconvolution of the amide-I band spectra in secondary structure components (antiparallel and parallel β-sheet, disordered conformation, α-helix, turn, and antiparallel β sheet), the spectrum of mature amyloid fibrils features a much more intense antiparallel and parallel β-sheet component, and a less-intense antiparallel component $(\beta\text{-sheet})_{AP}$, contrary to the spectrum of oligomers. This is in agreement with previous findings that αS oligomers and fibrils show an antiparallel (55,56) and parallel (57) β-sheet arrangement, respectively. It is worth remarking that, in the presence of a high density of ordered fibril agglomerates,

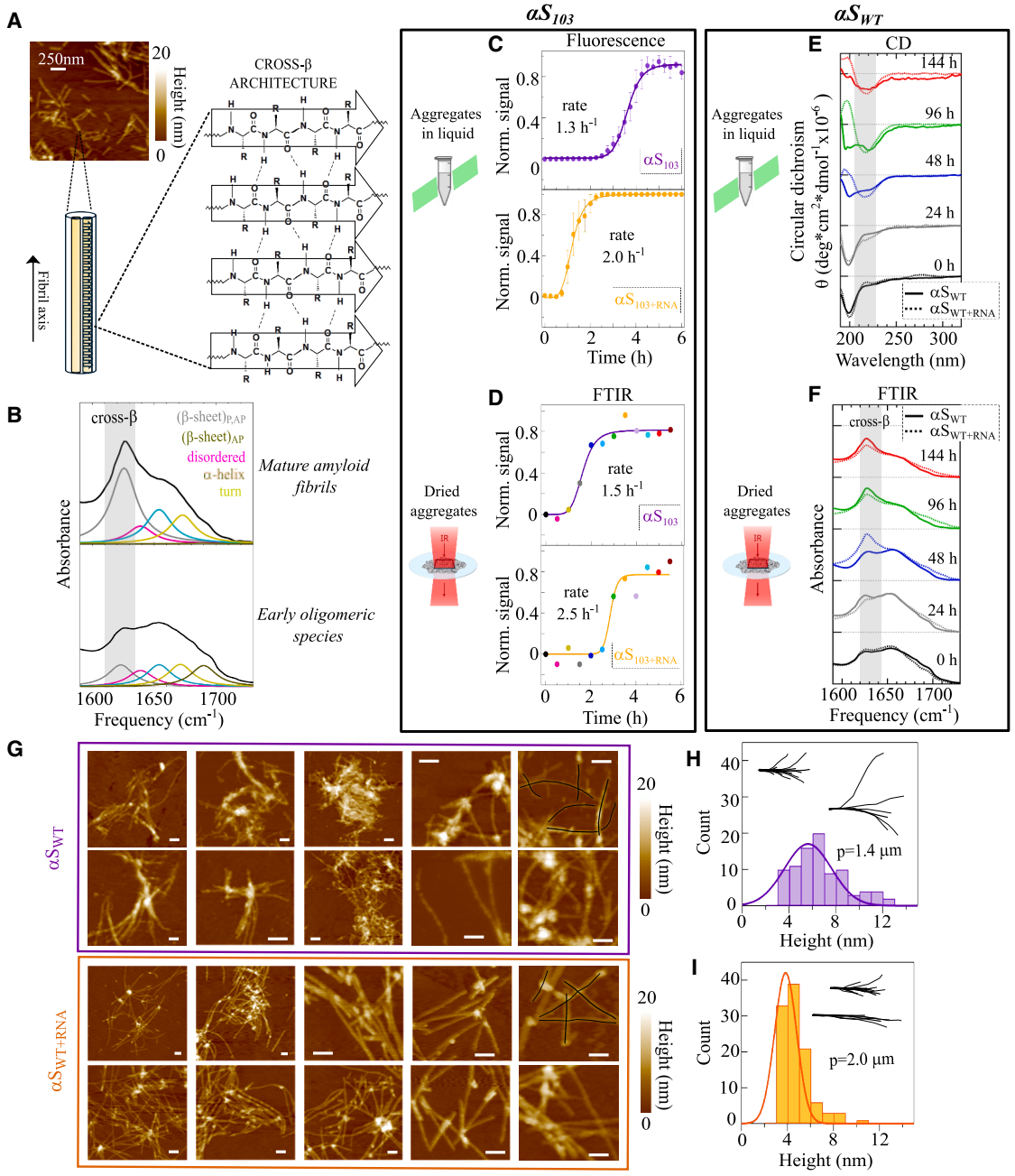

FIGURE 1 Effect of RNA on the fibril formation kinetics and morphology of αS fibrils. (*A*) Left: AFM image of αS fibrils with a schematic representation of the two protofibrils that constitute the fibril (70). The β-strands adopt a parallel and in-register arrangement and are perpendicular to the fibril axis (49). Right: schematics of the interstrand H-bond between the carbonyl and the amine groups in the peptide backbone, called cross-β architecture, detected by IR. (*B*) Amide-I band deconvolution of αS_{WT} fibrils (*top*) and oligomers (*bottom*) using five Lorentzian components centered at 1625, 1640, 1652, 1670, and 1690 cm^{-1}. Each Lorentzian component corresponds to a specific protein secondary structure based on its frequency position (41). (*C*) Experimental data from averaged time-resolved Proteostat™ fluorescence replicates of αS_{103} in the absence (*top*) and presence (*bottom*) of RNA with standard deviations. (*D*) Maximum percentage values of the FTIR $(\beta\text{-sheet})_{P,AP}$ component for the αS_{103} (*top*) and $\alpha S_{103+RNA}$ (*bottom*) samples. See Figs. S2 and S3 for representative FTIR spectra and trend of the amide-I band deconvolution components. The data in (*B*) and (*D*) were fitted into a sigmoidal curve using the Hill function. Best-fit aggregation rates for fluorescence (and FTIR) are 1.3 ± 0.1 h^{-1} (1.5 ± 0.4 h^{-1}) for αS_{103} and 2.0 ± 0.2 h^{-1} (2.5 ± 1.3 h^{-1}) for $\alpha S_{103+RNA}$ samples. (*E* and *F*) CD and micro-FTIR absorption spectra (200 × 200 μm^2 sample area) of αS_{WT} (*continuous line*) and αS_{WT+RNA} (*dashed line*) at different sampling times. The micro-FTIR spectra are normalized at 1660 cm^{-1}. (*G*) Contact-mode AFM topography maps of αS_{WT} (*top*) and αS_{WT+RNA} (*bottom*) fibrils. Scale bar, 200 nm. (*H* and *I*) Histograms of the height distribution of αS_{WT} (*H*) and αS_{WT+RNA} (*I*) fibrils (bin size is 1 nm). In the inset, the trajectory of fibrils with different lengths (superimposed black lines in the AFM images of (*G*)), where the tangents at the initial end are aligned.

the β-sheet component becomes representative of the supramolecular cross-β architecture, rather than just the secondary structure of the β-sheets, with a lineshape determined via the transition dipole coupling (TDC) (49,50). Hereafter, we refer to the antiparallel and parallel β-sheet peak as the cross-β peak.

In our case study, time-resolved fluorescence data revealed that RNA increases the αS aggregation rate, with a more pronounced effect observed for the αS_{103} isoform compared with αS_{WT} (Fig. S1) (24). We then performed IR spectroscopy experiments at various stages of in vitro aggregation process for both the αS_{WT} and αS_{103} isoforms (Figs. S2 and S3). Specifically, we monitored variations of the cross-β peak intensity as a function of aggregation time. For a direct comparison with fluorescence data, we calculated the normalized cross-β percentage values obtained from amide-I band deconvolution, and plotted them at various time points to obtain a similar kinetic plot. Importantly, we verified that the spectral contribution of RNA is negligible compared with that of proteins and therefore does not significantly affect the amide-I band. In Fig. 1, *C* and *D*, we provide a benchmark between the kinetic curves obtained by time-resolved fluorescence and FTIR data for the αS_{103} isoform in the presence and absence of RNA. Similar data for the wild-type protein are reported in Fig. S4, although in this case an evaluation of aggregation rates to be compared with those obtained from fluorescence data was not possible (see supporting material for data and relative discussion). To quantify the aggregation rate, we fitted both the time-resolved fluorescence (Fig. 1 *C*) and the cross-β peak intensity from FTIR (Fig. 1 *D*) and calculated the aggregation parameters as outlined in (24) (best-fitting rate values reported in the insets). Good agreement is obtained in terms of relative rate, with a higher value in the presence of RNA for both fluorescence and FTIR data. It is worth noting, however, that the latter two techniques are sensitive to different features of the aggregates and that in vitro aggregation was promoted under slightly different conditions, as reported in the materials and methods. These factors can justify possible differences both in terms of the absolute value of rates and lag phases, but the main point that RNA increases the aggregation rate is confirmed.

Further confirmation of the good comparison between experiments performed on deposited αS_{WT} aggregates and those in solution comes from benchmarking FTIR and CD spectra, which were acquired under the same aggregation conditions on the αS_{WT} only (see Fig. 1, *E* and *F*). Note that the sampling interval, ranging from 0 to 6 h for αS_{103}, was considerably shorter than the 0 to 144 h used for αS_{WT}, consistent with well-established findings that αS_{103} aggregates significantly faster than αS_{WT}, regardless of RNA presence in the aggregating solution (58,59). CD can be performed in solution and it is a label-free technique featuring structural sensitivity, although less specific than IR spectroscopy to the cross-β architecture. The intensity of the peak related to the β-sheet conformation (cross-β peak at 1625 cm^{-1} in the FTIR spectra and negative peak centered at 220 nm in the CD spectra) increases with an onset at the same time t for the αS_{WT} (96 h) and αS_{WT+RNA} (48 h) samples, pointing to the same RNA-mediated aggregation process.

Along the pathway of amyloid fibril formation, we conducted AFM analysis, which enables morphological investigation at the single fibril level, to monitor possible effects of RNA also on aggregate morphology (60–63). We focused on mature fibrils, which are the end products of the aggregation process. Consistent with reports from other groups on αS_{WT} (64–67), we observe a certain degree of variability in the morphology and dimension of aggregates obtained at a given sampling time in the wild-type samples. Despite this variability, we easily found micrometer-long amyloid fibrils in both αS_{WT} and αS_{WT+RNA} samples (see representative images in Fig. 1 *G*). As shown in the histograms in Fig. 1, *H* and *I*, on average, the height of αS_{WT+RNA} fibrils (4.4 ± 1.3 nm, number of analyzed fibrils $n = 106$) is lower than that of αS_{WT} fibrils (6.1 ± 2.9 nm, $n = 89$), and the height distribution is narrower in the presence of RNA. Additionally, amyloid fibrils forming in the presence of RNA display a larger curvature radius compared with αS_{WT} fibrils. This is evident from the comparison of representative fibril trajectories reported in the insets of Fig. 1, *H* and *I* and further confirmed by the calculated persistence length of 1.4 ± 0.2 μm ($n = 52$) for αS_{WT} and 2.0 ± 0.1 μm ($n = 51$) for αS_{WT+RNA} fibrils (Fig. S5). Although the calculated values are significantly different, one can envision strengthening this result by adopting surface functionalization methods to obtain isolated single fibrils and more precise values of the persistence length.

To understand the molecular mechanisms behind the observed morphological differences, as well as the distinct aggregation kinetics, we conducted extensive IR studies to gain insights into the architecture of mature aggregates grown in the presence or absence of RNA. We leveraged two great advantages of IR spectroscopy over other optical spectroscopies, including fluorescence and CD, to address the issue of polymorphism. First, IR spectroscopy allows for a drastic reduction of the probed volume, down to a few microns and nanometers, thus overcoming the limitations of volume-averaging approaches and allowing a direct benchmarking between the micro- and nanospectroscopic results. Second, it provides information on the architecture of the aggregates (not just their amount) through an in-depth analysis of the cross-β peak. Raman spectroscopy also provides label-free sensitivity to protein conformation, although less sensitive than IR spectroscopy, while enabling a similar multiscale approach (68,69). Given the complementary nature of the information provided by the two techniques, it would be interesting to extend this work in that direction in the future.

Low-polymorphic seed-amplified $\alpha S_{WT,seed}$ isoform

We started with αS_{WT}, which exhibits a low degree of fibril polymorphism and has been extensively studied using optical spectroscopies, scanning probe microscopies, and high-resolution structural techniques (33,70,71). We first conducted an analysis of the cross-β peak in the micro-FTIR spectra acquired from both αS_{WT} and αS_{WT+RNA} samples (Fig. S6). This analysis did not reveal any clear structural differences between the two samples, likely due to a combination of polymorphism and large probed areas. To amplify possible structural effects of RNA, we used the seed-amplified wild-type αS ($\alpha S_{WT,seed}$) in vitro assay, which relies on the intrinsic self-replicative nature of αS aggregates (seeds) (72). Amyloid fibrils grown in the absence and presence of free RNA in suspension were used as template structures for αS_{WT} monomers. Such a procedure is expected to exacerbate possible structural differences between amyloid fibrils formed starting from the two different templates, insofar as reducing the structural polymorphism. A further advantage of $\alpha S_{WT,seed}$ samples is that there is no free RNA in the aggregating solution, which can otherwise affect the high-frequency tail of the amide-I band (50). To increase statistics and gain deeper insights into structural heterogeneity, we acquired multiple micro-FTIR spectra, reducing the probed sample area compared with the micro-FTIR spectra reported in Fig. 1 (15×15 vs. $200 \times 200\ \mu m^2$). In Fig. 2, *A* and *B*, we report representative micro-FTIR spectra from $15 \times 15\ \mu m^2$ areas and their corresponding second-order derivatives. The second derivative of a band has a narrower line width compared with the original band, allowing for better resolution of overlapping bands within the amide-I region. The spectra were selected to emphasize the structural variability within each fibril population of the two samples ($\alpha S_{WT,seed}$ and $\alpha S_{WT+RNA,seed}$). In both samples, no distinct negative peak around 1690 cm^{-1} is observed in the second-order derivative curves (see Fig. 2 *B*). This suggests that the parallel β-sheet architecture, typical for αS_{WT} fibrils (57), is retained in the presence of RNA. However, it is evident that the two samples, $\alpha S_{WT,seed}$ and $\alpha S_{WT+RNA,seed}$, feature clear structural differences, primarily attributed to variations in the cross-β peak (highlighted in the figures by the *vertical gray shadow*). As indicated by the second-order derivative curves, the key difference in the cross-β peak between the two samples is that the central frequency of the principal negative peak, referred to as ω_β, is on average lower for $\alpha S_{WT+RNA,seed}$ compared with $\alpha S_{WT,seed}$. This frequency shift is accompanied by a slightly narrower negative peak (see Gaussian fit in the *inset* of Fig. 2 *B*), together with the appearance of a smaller negative peak centered below 1620 cm^{-1} in the second derivative curves of the $\alpha S_{WT+RNA,seed}$ spectra, which has been related to a stronger H-bond network (28, 73). Histograms of ω_β, along with PCA, derived from ∼100 micro-FTIR spectra for each sample (Fig. 2, *C* and *D*), confirm the significance of this observation despite the structural variability within each sample population (note that the PCA was performed within the frequency interval of 1605–1640 cm^{-1} to optimize the separation of the principal components). On the one hand, the histograms show a clear spectral transfer of the cross-β peak toward lower frequencies for $\alpha S_{WT+RNA,seed}$. In the insets of Fig. 2 *C*, we also report the average second-order derivative curves for spectra with $\omega_\beta < 1626.5$ cm^{-1} and $\omega_\beta > 1626.5$ cm^{-1}, confirming the correlation between the shift of ω_β toward lower frequencies and the increase in intensity of the small peak centered below 1620 cm^{-1}. On the other hand, in the PCA scores plot, the two fibril populations mainly differ in the value of the PC2 component, which crosses zero at 1625 cm^{-1}, suggesting that the main difference arises from the shift of ω_β (see PC1 and PC2 components in the loadings plots of the inset Fig. 2 *D*). RNA also appears to affect the heterogeneity within the aggregate population, as indicated by the narrower ω_β distribution in the histogram of $\alpha S_{WT+RNA,seed}$ (Fig. 2 *C, bottom*). To further validate this finding, we show the PCA scores plot in Fig. 2 *E*, derived from spectra obtained with a FPA detector, which enables the simultaneous acquisition of thousands of spectra from areas as small as a few square micrometers, with each pixel corresponding to an area of $2.7 \times 2.7\ \mu m^2$. In agreement with the ω_β histograms, the scatter plot for the $\alpha S_{WT,seed}$ shows two distinct clusters and is broader than that for $\alpha S_{WT+RNA,seed}$, pointing to a higher structural heterogeneity. Additionally, the AFM characterization in terms of fibril height shown earlier in Fig. 1, *H* and *I* is consistent with a lower degree of morphological heterogeneity in the presence of RNA. The overall data suggest that, within the polymorphic population, RNA somehow promotes certain fibril architectures that would otherwise be less likely (see the histograms of ω_β), insofar as reducing the degree of morphological and structural polymorphism.

IR nanospectroscopy applied to $\alpha S_{WT,seed}$ isoform

Besides micro-FTIR techniques, we also adopted IR nanospectroscopy approaches, both s-SNOM and AFM-IR, which enhance the structural sensitivity of IR spectroscopy at the nanoscale, ideally down to the single aggregate level (74–76). While spectra of individual fibrils can be acquired, our focus was on agglomerates of fibrils rather than on single fibrils. This is because the intensity—although not the frequency and width—of the cross-β peak in IR nanospectroscopy spectra of amyloid fibrils depends on the relative angle between the electric field in the nanogap and the mean C=O dipole moment, which can vary among different agglomerates (77). According to the selection rule that defines the physical process of IR absorption, a nonzero relative angle is required between the electric field and the dipole moment associated with the vibration. In the

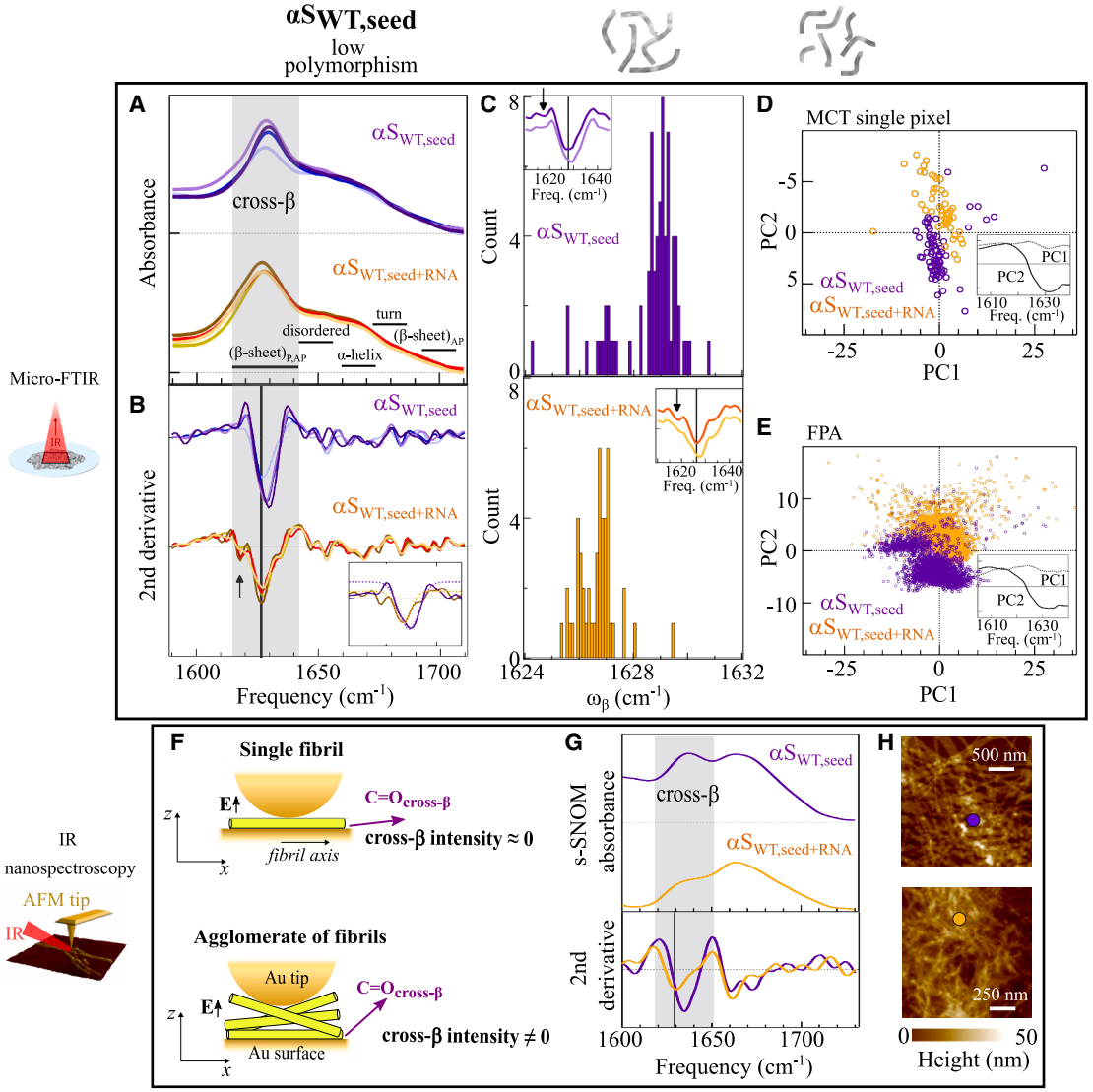

FIGURE 2 Effect of RNA on the supramolecular architecture of the less polymorphic $\alpha S_{WT,seed}$ fibrils. (*A* and *B*) Micro-FTIR absorption spectra (15 × 15 μm^2) with the assignment of the secondary structure components (*A*) and corresponding second-order derivative curves (*B*) for the $\alpha S_{WT,seed}$ (*purple line*) and $\alpha S_{WT+RNA,seed}$ (*orange line*). The inset of (*B*) shows representative second-order derivatives with Gaussian fits of the $(\beta\text{-sheet})_{P,AP}$ component. The Gaussian fits have a central frequency at 1629.3 and 1626.7 cm^{-1} and a FWHM of 5.4 and 4.3 cm^{-1} for the $\alpha S_{WT,seed}$ and $\alpha S_{WT+RNA,seed}$ curves, respectively. (*C*) Histogram of the ω_β distribution of $\alpha S_{WT,seed}$ (*top*) and $\alpha S_{WT+RNA,seed}$ (*bottom*) fibrils measured in 15 × 15 μm^2 areas (bin size is 0.1 cm^{-1}). Number of analyzed spectra is 73 (*top*) and 48 (*bottom*). In the insets, we show the average second-order derivatives from the low-frequency (<1626.5 cm^{-1}, *purple and red line*) and high-frequency (>1626.5 cm^{-1}, *light purple and orange line*) populations of the histograms. Arrows indicate the 1620 cm^{-1} contribution. (*D* and *E*) PCA scores plots showing a clear separation between the ω_β of $\alpha S_{WT,seed}$ and $\alpha S_{WT+RNA,seed}$ fibrils measured in 15 × 15 μm^2 areas with an MCT detector (*D*) and 2.7 × 2.7 μm^2 areas with an FPA detector (*E*). In the insets, the loadings plots show the PC1 and PC2 coordinates, which indicate the first and second principal components. PC1 and PC2 variance is 56% and 32% for FPA and 60% and 28% for MCT, respectively. (*F*) Sketch of the relative angle between the electric field in the tip-gold nanogap and the C=O cross-β dipole moment for a simplified case of an individual rod-like amyloid fibril (*top*) and an agglomerate of fibrils (*bottom*). (*G*) s-SNOM absorbance spectra (*top*) and corresponding second-order derivative curves (*bottom*) of $\alpha S_{WT,seed}$ (*purple line*) and $\alpha S_{WT+RNA,seed}$ (*orange line*) fibril agglomerates. Spectra are the average of measurements at four different locations of the fibril agglomerates. (*H*) AFM topography maps of the $\alpha S_{WT,seed}$ (*top*) and $\alpha S_{WT+RNA,seed}$ (*bottom*) fibril agglomerates where the s-SNOM spectra were acquired.

tip-gold nanogap, the electric field is expected to be almost fully vertical, while the dipole moment of the C=O stretching of parallel and antiparallel β-sheet in single fibrils has a small vertical component (see simplified sketch in Fig. 2 *F* reporting the ideal case of a single rod fibril). This results in a low-intensity but still measurable cross-β peak (74) in the case of individual fibrils, as we also experimentally confirmed (data not shown), hence making challenging an accurate analysis of this peak (77). Note that this is not the case for the high-frequency antiparallel β-sheet peak. On the contrary, on the agglomerate of fibrils, there is a significant vertical component of the total C=O dipole moment

due to the imperfect planar orientation of the fibrils and therefore the cross-β peak is pronounced. In this work, we focused on agglomerates, as their higher cross-β peak intensity enhances the accuracy of the central frequency analysis.

In the top of Fig. 2 *G*, we show two representative s-SNOM spectra acquired on agglomerates of $\alpha S_{WT,seed}$ and $\alpha S_{WT+RNA,seed}$ amyloid fibrils (see the AFM topography maps in Fig. 2 *H*), both featuring a clear and distinguishable cross-β peak. The reported spectra were obtained by averaging measurements at different locations within the same fibril agglomerates. By comparing the second-order derivative curves of the two average s-SNOM spectra (Fig. 2 *G*, *bottom*), one can see that the main difference appears in the frequency interval of the cross-β peak. More importantly, $\alpha S_{WT+RNA,seed}$ fibrils clearly show a lower value of ω_β, in perfect agreement with the micro-FTIR data (Fig. 2 *B*). The absence of a clear small peak centered below 1620 cm^{-1} can be ascribed to the lower spectral resolution, as well as the lower SNR of the s-SNOM spectra (and all AFM-based IR nanospectroscopy approaches) compared with FTIR. Such IR nanospectroscopy experiments further confirm that the amyloid fibrils grown in the presence or absence of RNA feature structural differences arising from diverse supramolecular architectures, insofar as explaining micro-FTIR results with nanometric detail.

Polymorphic C-truncated αS_{103} isoform

The low degree of fibril polymorphism in αS_{WT} enabled us to employ micro-FTIR technique, which provided high SNR spectra, while simultaneously gaining a global picture of possible heterogeneity through FPA detection. We now aim to investigate the structural effects of RNA on the pathologically relevant αS_{103} isoform (25), for which the large polymorphism poses challenges when using bulk techniques due to volume-averaging effects. By performing the same analysis on the αS_{103} and $\alpha S_{103+RNA}$ samples as we did for the micro-FTIR data of the seed-amplified wild-type protein samples, we observed only subtle differences between the two samples (see the PCA scores plots and histograms of ω_β reported in Fig. 3, *A* and *B*). These very small differences may be attributed to averaging effects over structurally different aggregates, on which RNA potentially has varying impacts. It is important to note that a systematic morphological analysis, in terms of height and persistence length of individual αS_{103} fibrils, was not feasible for the truncated isoform of αS because of its high degree of fibril polymorphism and formation of large fibril bundles, as also reported in the literature for C-terminally truncated isoforms of αS (78–80). Although αS_{103} has a higher seeding capacity (25) compared with αS_{WT}, it is known that αS_{103} seed fibrils do not effectively serve as templates for fibril elongation in the presence of αS_{103} monomers (59). We therefore conducted experiments exclusively on αS_{103} and $\alpha S_{103+RNA}$, for which investigation at the nanoscale level becomes of paramount relevance for unraveling the effect of RNA on the diverse polymorphs.

IR-Nanospectroscopy applied to polymorphic C-truncated αS_{103} isoform

We employed photothermal-expansion AFM-IR nanospectroscopy, which, for thin samples placed in the nanogap formed by a metallic AFM probe tip and a metallic surface (tip-gold nanogap), offers sensitivity down to nanometer-sized samples (81–83), similarly to s-SNOM. In Fig. 3, *C* and *D*, extensive AFM and AFM-IR analysis revealed significant morphological variability in probed samples featuring an amide-I band with a pronounced cross-β peak, indicative of mature protein aggregates, in both αS_{103} and $\alpha S_{103+RNA}$ samples. Interestingly, we observed not only micrometer-long fibrils but also a variety of less-ordered aggregates, such as amorphous ones, forming under the same aggregating conditions. This morphological diversity of the αS_{103} aggregates aligns with previous reports on other C-terminal truncations of αS (78–80), which also confirm the propensity of such an isoform to form fibril agglomerates/bundles, as observed in Fig. 3, *C* and *D*.

To monitor potential structural effects induced by RNA, we calculated the second derivative curves for AFM-IR spectra displaying a clear and distinguishable cross-β peak (see Fig. 3 *E*). We then fitted the negative second derivative peak associated with the cross-β peak using a Gaussian line shape. In Fig. 3 *F*, we show the correlation plot of ω_β (central frequency of the Gaussian curve) versus the FWHM of the Gaussian curve. On average, $\alpha S_{103+RNA}$ features lower values of the ω_β and a narrower FWHM compared with αS_{103} (see *circles* in Fig. 3 *F*), in line with observations for the seed-amplified wild-type isoform (see *inset* of Fig. 2 *B*). However, the difference between the two samples (with and without RNA) is much less pronounced for the C-truncated isoform. The advantage of such a high-resolution IR spectroscopic probe compared with bulk techniques, including micro-FTIR, lies in its ability to correlate, at the nanoscale, aggregate morphology with supramolecular architecture via the spectroscopic information. In Fig. 4, *A* and *C*, we compare the second derivative curves of αS_{103} and $\alpha S_{103+RNA}$ samples featuring similar morphologies, namely micrometer-long fibril agglomerates (Fig. 4 *D*) and amorphous, filament-shaped agglomerates that are thinner and less ordered (Fig. 4 *B*). It is evident that, for $\alpha S_{103+RNA}$ micrometer-long fibrils, the negative peak related to the cross-β peak displays a lower ω_β and a narrower FWHM. For amorphous aggregates, there is a subtle frequency shift and almost no variation of the peak width. This suggests that the more ordered the aggregate architecture appears (such as micrometer-long fibrils), the stronger the structural impact of RNA, with a tendency to induce the formation of even more rigid and compact supramolecular structures, as observed for the

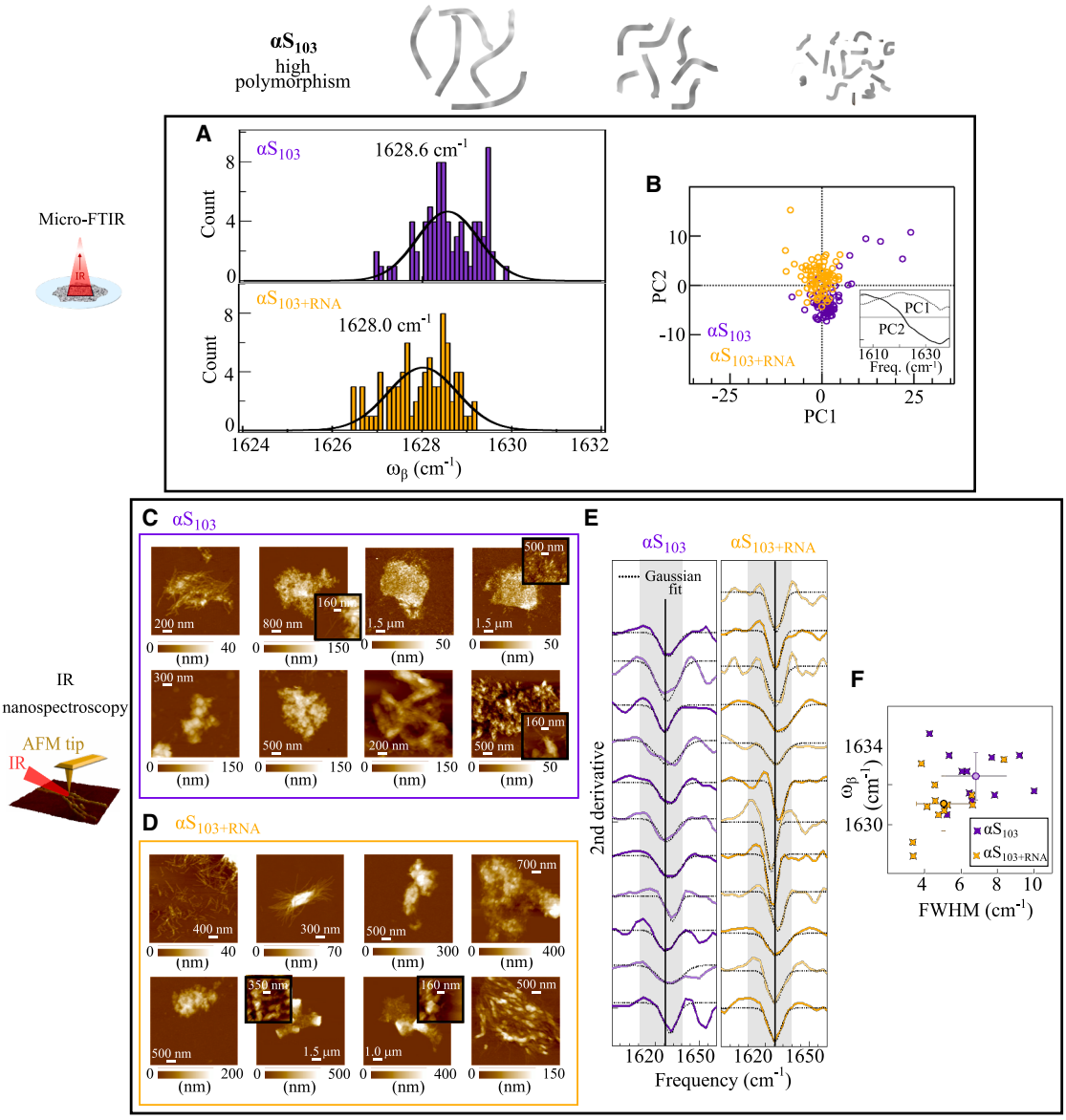

FIGURE 3 Effect of RNA on the morphology and supramolecular architecture of the highly polymorphic αS_{103} aggregates. (*A*) Histogram of the ω_β distribution of αS_{103} (*top*) and $\alpha S_{103+RNA}$ (*bottom*) fibrils measured in 15 × 15 μm^2 areas (bin size is 0.1 cm^{-1}). Number of analyzed spectra is 79 (*top*) and 82 (*bottom*). (*B*) PCA scores plot showing very little separation between the ω_β of αS_{103} and $\alpha S_{103+RNA}$ fibrils. In the inset, the loading plot shows the PC1 and PC2 coordinates, which indicate the first and second principal components. PC1 and PC2 variance is 51 and 42%, respectively. (*C* and *D*) AFM topography maps of αS_{103} (*C*) and $\alpha S_{103+RNA}$ (*D*) agglomerate of amorphous aggregates and fibrils. (*E*) Second-order derivatives of AFM-IR spectra acquired on αS_{103} (*left*) and $\alpha S_{103+RNA}$ (*right*) amorphous aggregates and fibrils. The dashed lines are the Gaussian fits of the cross-β negative peak. (*F*) Plot of the ω_β of the Gaussian fit versus the Gaussian FWHM for the αS_{103} and $\alpha S_{103+RNA}$ amorphous aggregates and fibrils in (*E*). Circle markers show the average values corresponding to the αS_{103} and $\alpha S_{103+RNA}$ samples. Horizontal and vertical error bars represent the standard deviation of the FWHM and $\omega_{cross-\beta}$, respectively. The average $\omega_{cross-\beta}$ values for αS_{103} and $\alpha S_{103+RNA}$ are 1633 ± 1 cm^{-1} and 1631 ± 1 cm^{-1}, respectively. Meanwhile, the average FWHM values are 7 ± 2 cm^{-1} and 5 ± 2 cm^{-1}, respectively. The total number of analyzed AFM-IR spectra is 11 for the αS_{103} and 12 for the $\alpha S_{103+RNA}$ samples.

seeded samples (Fig. 2). On amorphous, protofibril-like supramolecular structures, an almost negligible impact of RNA is observed. According to this result, the micro-FTIR data can be explained as effectively averaging over structurally different αS_{103} aggregates where the impact of RNA is different, thus providing almost identical "bulk" micro-FTIR spectra (Fig. 3, *A* and *B*).

DISCUSSION

Hypotheses about the main structural characteristics of the supramolecular architecture promoted by the coincubation with RNA can be made based on the IR data presented in the previous sections. It is well known that both the frequency and width of the cross-β peak are dependent on

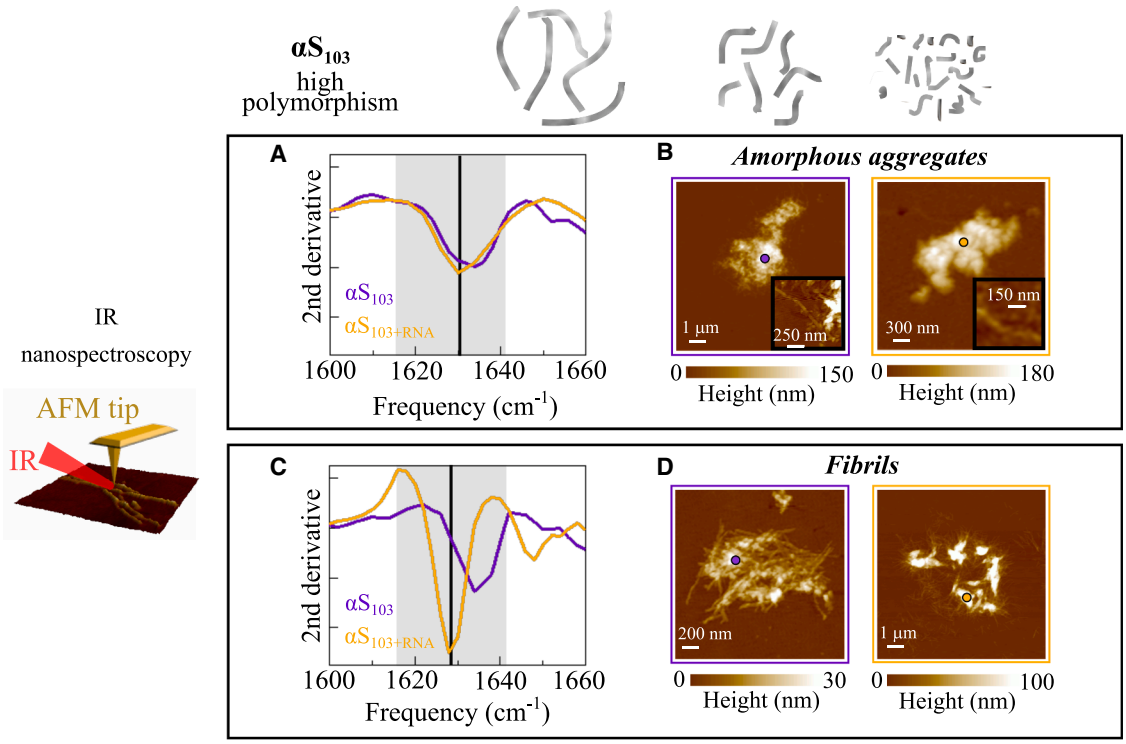

FIGURE 4 RNA has different structural effects on αS_{103} aggregates with distinct conformations. (*A* and *C*) Second-order derivatives of AFM-IR spectra acquired on αS_{103} and $\alpha S_{103+RNA}$ amorphous aggregates (*A*) and ordered fibrils (*C*). (*B* and *D*) AFM topography maps of αS_{103} and $\alpha S_{103+RNA}$ amorphous aggregates (*B*) and fibrils (*D*) . Filled circle markers on the AFM maps indicate the location where the AFM-IR spectra were acquired.

the architecture of the polypeptide backbone (84,85) via the TDC, which defines the coupling between vibrational modes of neighboring peptides (50). According to the TDC theory, the strength of this coupling depends on the specific protein arrangement along the fibril chain. Typically, the most ordered, compact, and rigid amyloid fibrils feature a narrower cross-β peak centered at a lower frequency when compared with the more disordered ones (49).

In the case of the low-polymorphic seed-amplified samples, the lower value of $\omega_{cross-\beta}$ obtained for $\alpha S_{WT+RNA,seed}$, together with AFM analysis showing increased persistence length of fibrils formed in the presence of RNA, suggests that RNA promotes the formation of more ordered, compact, and rigid fibrils. Different possible conditions can result in more rigid fibrils featuring a shift of the cross-β peak to lower frequencies, including increased H-bonding, more planar β-sheets, or a larger number of β-strands (51, 73). According to our data, one can hypothesize that the main effect of RNA is an increase of H-bond strength between the β-strands along the fibril axis (see sketch in Fig. 1 *A*). In (86), it has been demonstrated that the major contribution to the rigidity of amyloid fibrils stems from intermolecular forces, primarily in the form of an interbackbone H-bonding network characteristic of the cross-β structure. The same reference, together with subsequent ones (60,62), also suggests a positive correlation between the strength of interbackbone H-bonding and the persistence length of amyloid fibrils. Further corroboration of our hypothesis comes from the presence of the small negative peak around 1620 cm^{-1} in the second derivative curves for the $\alpha S_{WT+RNA,seed}$ sample (see Fig. 2 *B*), which is known to be related to an H-bond type featuring higher strength (28,73). In Fig. 5 *C*, we report a simplified sketch that depicts the structural effect of RNA, showing an increase in the H-bond between β-strands, represented as a decrease in the H-O distance of the carbonyl and amine groups in the peptide backbone. Given the supramolecular architecture of αS fibrils, it is reasonable to assume that, besides a tighter packing of the proteins along the fibril axis, the proteins are more compact also in the perpendicular direction, leading to a lower value of the fibril diameter (Fig. 1 *I*) when incubated with RNA. For the polymorphic C-truncated αS_{103} sample, the observed effect, when present, is still consistent with an increase of the intermolecular forces. Using the results from the template seed-amplified sample as a benchmark, one can reasonably hypothesize that RNA leads to the formation of more rigid and more ordered fibrils, even for the αS_{103} isoform. However, high-resolution AFM morphological characterization and direct AFM mechanical measurements (87,88) are required to confirm this hypothesis. Finally, for the low-polymorphic seed-amplified samples, where we were able to use a more "bulk" technique such as micro-FTIR to capture a global picture of structural heterogeneity, the overall data suggest

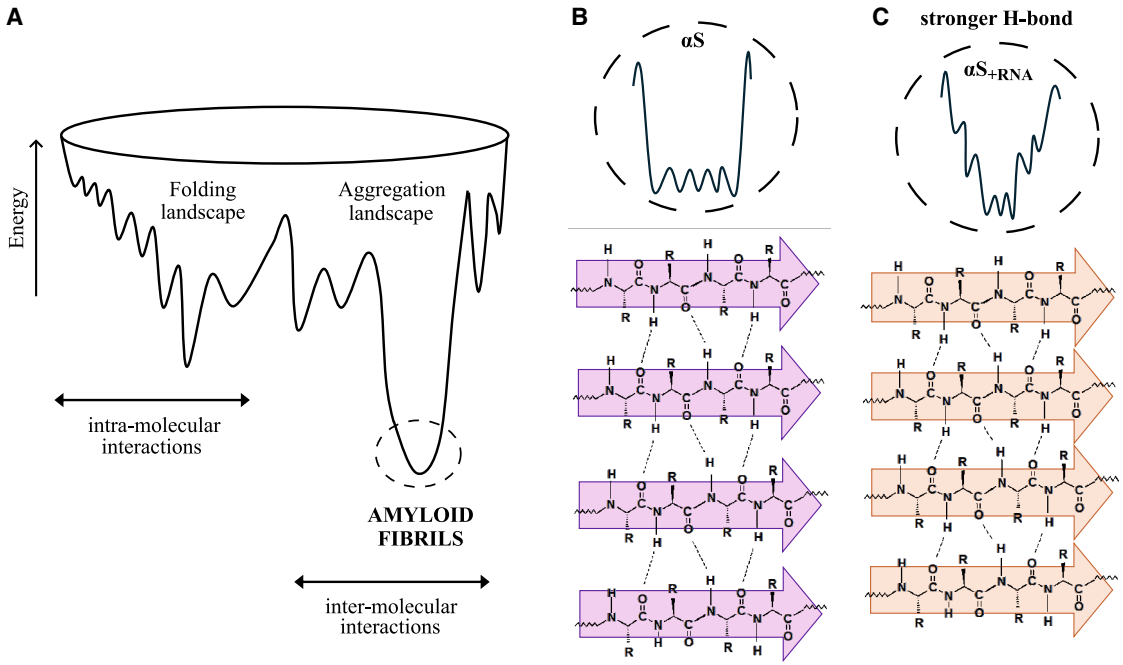

FIGURE 5 RNA favors the formation of stronger H-bonding among the β-sheets in the αS fibril structure. (*A*) Energy landscape of protein folding and aggregation. (*B* and *C*) Distribution of the low-energy levels related to fibril formation (*top*) and general chemical structure of β-strands (*bottom*), inside the αS (*B*) and αS_{+RNA} (*C*) fibril, interacting by H-bonds. In the presence of RNA, the H-bond network is stronger (represented by *thick dashed lines*).

that the presence of RNA may promote a specific structural architecture of fibrils within the polymorphic population (see sketch in Fig. 5). This structural effect (as indicated by the histograms and PCA scores plot of ω_β in Fig. 2) seems to reduce the degree of structural polymorphism.

In the case of αS, the perturbation of intra- and intermolecular forces between the N- and C-termini of the monomeric protein can strongly influence its aggregation propensity. Presumably, RNA interferes with these contacts, leading to an increased exposure of the hydrophobic central core region and an observed increase in the aggregation propensity of αS (24). We confirm these results in terms of aggregation kinetics and, in addition, we observe that coincubation with RNA potentially leads to a more rigid fibril structure, both for αS_{WT} and αS_{103}. The case of αS_{103} is particularly interesting because of the presence of what seem to be amorphous aggregates. These exhibit similar structural features both in the absence and presence of RNA, while the amyloid fibrils appear to be much more rigid and compact upon coincubation with RNA. Therefore, possibly in the case of "ordered" structures, such as amyloid fibrils, the effect of RNA is much more pronounced. This correlates well with the other major finding, namely that amyloids and particularly those of αS exhibit a much higher RNA binding propensity (24). While the original study did not involve any structural characterization of the resulting aggregates, we can now conclude from our observations that a higher RNA binding propensity is correlated with a higher conformational impact and a decreased polymorphism. Aggregate polymorphism is of particular concern for αS, since two structures of patient brain-derived amyloids exhibit significant differences, indicating that distinct amyloid folds are disease specific (89,90). Studying these structural transitions and developing novel approaches to decipher these structural changes can therefore be critical for advancing our understanding of disease and for designing effective diagnostic tools.

CONCLUSION

In conclusion, we have studied the effect of RNA on the supramolecular architecture of αS amyloid aggregates by leveraging the label-free sensitivity of IR spectroscopy to the cross-β architecture of protein fibrils. Combining statistical data obtained by means of IR microspectroscopy on a few micrometer-square areas with results obtained at the nanoscale using the ultrasensitive IR nanospectroscopy approach, we could reach an in-depth picture of the structural effect of RNA on the αS fibrils, when αS is coincubated with RNA. The observed structural effect is consistent with enhanced intermolecular forces, likely via a stronger H-bond network stabilizing the cross-β architecture of the αS fibrils. For the polymorphic C-truncated αS_{103} isoform, IR nanospectroscopy has proven fundamental to show that the greater the order of aggregates, the stronger the structural impact of RNA. Finally, a reduction in the degree of polymorphism within the aggregate population was observed when αS aggregation occurred in the presence of

RNA. Our work represents an important step forward in the understanding of RNA impacts on the structural and morphological properties of αS fibrils. Shedding light on these phenomena is relevant to the pathological implications of neurodegenerative diseases associated with the intracellular amyloid formation that can potentially sequester RNA.

ACKNOWLEDGMENTS

The authors thank Helmholtz-Zentrum Berlin für Materialien und Energie for the micro-FTIR and s-SNOM measurements carried out at the IRIS beamline of BESSY II in the framework of the HZB proposals 231-11769-ST. and 232-12355-ST-1.1-P. L.P., U.S., and A.V. acknowledge the funding by the German Federal Ministry for Education and Research (BMBF) project 05K19KH1 (SyMS). J.R., E.Z., and G.G.T. also acknowledge the funding through the grants ERC ASTRA_855923 (to G.G.T.) and PNRR grant from National Center for Gene Therapy and Drugs based on RNA Technology CN00000041, EPNRRCN3 (to G.G.T.).

AUTHOR CONTRIBUTIONS

G.G.T. designed the research. A.I., V.G., R.P., M.E.T., and M.O. performed the IR and AFM experiments and analyzed the data. J.R. and E.Z. prepared the protein samples and performed the CD experiments and protein aggregation assays. A.V., L.P., and U.S. contributed analytical tools. A.I. and V. G. wrote the article. All authors reviewed the results and approved the final version of the manuscript.

DECLARATION OF INTERESTS

The authors declare no competing interests.

SUPPORTING MATERIAL

Supporting material can be found online at https://doi.org/10.1016/j.bpj.2025.04.031.

REFERENCES

1. Louros, N., J. Schymkowitz, and F. Rousseau. 2023. Mechanisms and pathology of protein misfolding and aggregation. *Nat. Rev. Mol. Cell Biol.* 24:912–933.
2. Yavich, L., H. Tanila, …, P. Jäkälä. 2004. Role of α-synuclein in presynaptic dopamine recruitment. *J. Neurosci.* 24:11165–11170.
3. Vekrellis, K., M. Xilouri, …, L. Stefanis. 2011. Pathological roles of α-synuclein in neurological disorders. *Lancet Neurol.* 10:1015–1025.
4. Lashuel, H. A., C. R. Overk, …, E. Masliah. 2013. The many faces of α-synuclein: from structure and toxicity to therapeutic target. *Nat. Rev. Neurosci.* 14:38–48.
5. Galvin, J. E., V. M. Lee, and J. Q. Trojanowski. 2001. Synucleinopathies: clinical and pathological implications. *Arch. Neurol.* 58:186–190.
6. Luk, K. C., V. Kehm, …, V. M.-Y. Lee. 2012. Pathological α-synuclein transmission initiates Parkinson-like neurodegeneration in nontransgenic mice. *Science.* 338:949–953.
7. Uversky, V. N., J. Li, and A. L. Fink. 2001. Evidence for a partially folded intermediate in α-synuclein fibril formation. *J. Biol. Chem.* 276:10737–10744.
8. Fujiwara, S., F. Kono, …, K. Shibata. 2019. Dynamic properties of human α-synuclein related to propensity to amyloid fibril formation. *J. Mol. Biol.* 431:3229–3245.
9. Vendruscolo, M., T. P. J. Knowles, and C. M. Dobson. 2011. Protein solubility and protein homeostasis: a generic view of protein misfolding disorders. *Cold Spring Harbor Perspect. Biol.* 3:a010454.
10. Knowles, T. P. J., M. Vendruscolo, and C. M. Dobson. 2014. The amyloid state and its association with protein misfolding diseases. *Nat. Rev. Mol. Cell Biol.* 15:384–396.
11. Chiti, F., and C. M. Dobson. 2006. Protein misfolding, functional amyloid, and human disease. *Annu. Rev. Biochem.* 75:333–366.
12. Pedersen, J. S., D. Dikov, …, D. E. Otzen. 2006. The changing face of glucagon fibrillation: structural polymorphism and conformational imprinting. *J. Mol. Biol.* 355:501–523.
13. Buell, A. K., C. Galvagnion, …, C. M. Dobson. 2014. Solution conditions determine the relative importance of nucleation and growth processes in α-synuclein aggregation. *Proc. Natl. Acad. Sci.* 111:7671–7676.
14. Conway, K. A., J. D. Harper, and P. T. Lansbury. 2000. Fibrils formed in vitro from α-synuclein and two mutant forms linked to Parkinson's disease are typical amyloid. *Biochemistry.* 39:2552–2563.
15. Grey, M., S. Linse, …, E. Sparr. 2011. Membrane interaction of α-synuclein in different aggregation states. *J. Parkinsons Dis.* 1:359–371.
16. Burke, K. A., E. A. Yates, and J. Legleiter. 2013. Biophysical insights into how surfaces, including lipid membranes, modulate protein aggregation related to neurodegeneration. *Front. Neurol.* 4:17.
17. Brown, J. W. P., G. Meisl, …, C. Galvagnion. 2018. Kinetic barriers to α-synuclein protofilament formation and conversion into mature fibrils. *Chem. Commun.* 54:7854–7857.
18. Galvagnion, C., A. K. Buell, …, C. M. Dobson. 2015. Lipid vesicles trigger α-synuclein aggregation by stimulating primary nucleation. *Nat. Chem. Biol.* 11:229–234.
19. Roeters, S. J., A. Iyer, …, S. Woutersen. 2017. Evidence for intramolecular antiparallel beta-sheet structure in alpha-synuclein fibrils from a combination of two-dimensional infrared spectroscopy and atomic force microscopy. *Sci. Rep.* 7:41051.
20. Yoshimura, Y., Y. Lin, …, Y. Goto. 2012. Distinguishing crystal-like amyloid fibrils and glass-like amorphous aggregates from their kinetics of formation. *Proc. Natl. Acad. Sci.* 109:14446–14451.
21. Munishkina, L. A., J. Henriques, …, A. L. Fink. 2004. Role of protein-water interactions and electrostatics in α-synuclein fibril formation. *Biochemistry.* 43:3289–3300.
22. Fink, A. L. 2006. Factors Affecting the Fibrillation of α-Synuclein, a Natively Unfolded Protein. Springer, New York, NY, pp. 265–285.
23. Wu, C., M. Bagnani, …, R. Mezzenga. 2024. Cholesteric Tactoids with Tunable Helical Pitch Assembled by Lysozyme Amyloid Fibrils. *Small.* 20:e2305839.
24. Rupert, J., M. Monti, …, G. G. Tartaglia. 2023. RNA sequestration driven by amyloid formation: the alpha synuclein case. *Nucleic Acids Res.* 51:11466–11478.
25. Zhang, Z., S. S. Kang, …, K. Ye. 2017. Asparagine endopeptidase cleaves α-synuclein and mediates pathologic activities in Parkinson's disease. *Nat. Struct. Mol. Biol.* 24:632–642.
26. Bhopatkar, A. A., and R. Kayed. 2023. Flanking regions, amyloid cores, and polymorphism: the potential interplay underlying structural diversity. *J. Biol. Chem.* 299:105122.
27. Zagrovic, B., L. Bartonek, and A. A. Polyansky. 2018. RNA-protein interactions in an unstructured context. *FEBS Lett.* 592:2901–2916.
28. Ziaunys, M., A. Sakalauskas, …, V. Smirnovas. 2021. Polymorphism of alpha-synuclein amyloid fibrils depends on ionic strength and protein concentration. *Int. J. Mol. Sci.* 22:12382.
29. Tao, Y., Y. Sun, …, D. Li. 2022. Heparin induces α-synuclein to form new fibril polymorphs with attenuated neuropathology. *Nat. Commun.* 13:4226.
30. Zacco, E., R. Graña-Montes, …, A. Pastore. 2019. RNA as a key factor in driving or preventing self-assembly of the TAR DNA-binding protein 43. *J. Mol. Biol.* 431:1671–1688.

31. Abskharon, R., M. R. Sawaya, …, D. S. Eisenberg. 2022. Cryo-EM structure of RNA-induced tau fibrils reveals a small C-terminal core that may nucleate fibril formation. *Proc. Natl. Acad. Sci.* 119: e2119952119.

32. Dinkel, P. D., M. R. Holden, …, M. Margittai. 2015. RNA binds to tau fibrils and sustains template-assisted growth. *Biochemistry.* 54:4731–4740.

33. Tuttle, M. D., G. Comellas, …, C. M. Rienstra. 2016. Solid-state NMR structure of a pathogenic fibril of full-length human α-synuclein. *Nat. Struct. Mol. Biol.* 23:409–415.

34. Coles, N. P., S. Elsheikh, …, A. A. Khundakar. 2025. Molecular Insights into α-Synuclein Fibrillation: A Raman Spectroscopy and Machine Learning Approach. *ACS Chem. Neurosci.* 16:687–698.

35. Pachetti, M., F. D'Amico, …, C. Masciovecchio. 2021. UV Resonance Raman explores protein structural modification upon fibrillation and ligand interaction. *Biophys. J.* 120:4575–4589.

36. Eremina, O. E., N. R. Yarenkov, …, I. A. Veselova. 2024. Silver nanoparticle-based SERS sensors for sensitive detection of amyloid-β aggregates in biological fluids. *Talanta.* 266:124970.

37. Sofińska, K., S. Seweryn, …, E. Lipiec. 2024. Tip-enhanced Raman spectroscopy reveals the structural rearrangements of tau protein aggregates at the growth phase. *Nanoscale.* 16:5294–5301.

38. Ami, D., P. Mereghetti, and A. Natalello. 2022. Contribution of infrared spectroscopy to the understanding of amyloid protein aggregation in complex systems. *Front. Mol. Biosci.* 9:822852.

39. Jahn, T. R., G. A. Tennent, and S. E. Radford. 2008. A common β-sheet architecture underlies in vitro and in vivo β2-microglobulin amyloid fibrils. *J. Biol. Chem.* 283:17279–17286.

40. Biancalana, M., and S. Koide. 2010. Molecular mechanism of Thioflavin-T binding to amyloid fibrils. *Biochim. Biophys. Acta.* 1804:1405–1412.

41. Shenoy, J., N. El Mammeri, …, A. Loquet. 2020. Structural dissection of amyloid aggregates of TDP-43 and its C-terminal fragments TDP-35 and TDP-16. *FEBS J.* 287:2449–2467.

42. Toplak, M., S. T. Read, …, F. Borondics. 2021. Quasar: easy machine learning for biospectroscopy. *Cells.* 10:2300.

43. Fellows, A. P., M. T. L. Casford, and P. B. Davies. 2020. Infrared nanospectroscopy of air-sensitive biological substrates protected by thin hydrogel films. *Biophys. J.* 119:1474–1480.

44. Mayet, C., A. Dazzi, …, J. M. Ortega. 2008. Sub-100 nm IR spectromicroscopy of living cells. *Opt. Lett.* 33:1611–1613.

45. Jin, M., F. Lu, and M. A. Belkin. 2017. High-sensitivity infrared vibrational nanospectroscopy in water. *Light Sci. Appl.* 6:e17096.

46. Ramer, G., F. S. Ruggeri, …, A. Centrone. 2018. Determination of polypeptide conformation with nanoscale resolution in water. *ACS Nano.* 12:6612–6619.

47. Eisenberg, D., and M. Jucker. 2012. The amyloid state of proteins in human diseases. *Cell.* 148:1188–1203.

48. Jahn, T. R., O. S. Makin, …, L. C. Serpell. 2010. The common architecture of cross-β amyloid. *J. Mol. Biol.* 395:717–727.

49. Moran, S. D., and M. T. Zanni. 2014. How to get insight into amyloid structure and formation from infrared spectroscopy. *J. Phys. Chem. Lett.* 5:1984–1993.

50. Barth, A., and C. Zscherp. 2002. What vibrations tell about proteins. *Q. Rev. Biophys.* 35:369–430.

51. Sarroukh, R., E. Goormaghtigh, …, V. Raussens. 2013. ATR-FTIR: A "rejuvenated" tool to investigate amyloid proteins. *Biochim. Biophys. Acta.* 1828:2328–2338.

52. Hahn, S., S.-S. Kim, …, M. Cho. 2005. Characteristic two-dimensional IR spectroscopic features of antiparallel and parallel β-sheet polypeptides: Simulation studies. *J. Chem. Phys.* 123:084905.

53. Shivu, B., S. Seshadri, …, A. L. Fink. 2013. Distinct β-sheet structure in protein aggregates determined by ATR–FTIR spectroscopy. *Biochemistry.* 52:5176–5183.

54. Zandomeneghi, G., M. R. H. Krebs, …, M. Fändrich. 2004. FTIR reveals structural differences between native β-sheet proteins and amyloid fibrils. *Protein Sci.* 13:3314–3321.

55. Celej, M. S., R. Sarroukh, …, V. Raussens. 2012. Toxic prefibrillar α-synuclein amyloid oligomers adopt a distinctive antiparallel β-sheet structure. *Biochem. J.* 443:719–726.

56. Cerf, E., R. Sarroukh, …, V. Raussens. 2009. Antiparallel β-sheet: a signature structure of the oligomeric amyloid β-peptide. *Biochem. J.* 421:415–423.

57. Der-Sarkissian, A., C. C. Jao, …, R. Langen. 2003. Structural organization of α-synuclein fibrils studied by site-directed spin labeling. *J. Biol. Chem.* 278:37530–37535.

58. Sorrentino, Z. A., and B. I. Giasson. 2020. The emerging role of α-synuclein truncation in aggregation and disease. *J. Biol. Chem.* 295:10224–10244.

59. van der Wateren, I. M., T. P. J. Knowles, …, C. Galvagnion. 2018. C-terminal truncation of α-synuclein promotes amyloid fibril amplification at physiological pH. *Chem. Sci.* 9:5506–5516.

60. Sasanian, N., R. Sharma, …, F. Westerlund. 2023. Probing physical properties of single amyloid fibrils using nanofluidic channels. *Nanoscale.* 15:18737–18744.

61. Schleeger, M., C. C. vandenAkker, …, M. Bonn. 2013. Amyloids: from molecular structure to mechanical properties. *Polymer.* 54:2473–2488.

62. vandenAkker, C. C., M. F. M. Engel, …, G. H. Koenderink. 2011. Morphology and persistence length of amyloid fibrils are correlated to peptide molecular structure. *J. Am. Chem. Soc.* 133:18030–18033.

63. Gosal, W. S., I. J. Morten, …, S. E. Radford. 2005. Competing pathways determine fibril morphology in the self-assembly of β2-microglobulin into amyloid. *J. Mol. Biol.* 351:850–864.

64. Zhou, L., and D. Kurouski. 2020. Structural characterization of individual α-synuclein oligomers formed at different stages of protein aggregation by atomic force microscopy-infrared spectroscopy. *Anal. Chem.* 92:6806–6810.

65. Makky, A., L. Bousset, …, R. Melki. 2016. Nanomechanical properties of distinct fibrillar polymorphs of the protein α-synuclein. *Sci. Rep.* 6:37970.

66. Yang, X., J. K. Williams, …, J. Baum. 2019. Increased dynamics of α-synuclein fibrils by β-synuclein leads to reduced seeding and cytotoxicity. *Sci. Rep.* 9:17579.

67. Ruggeri, F. S., F. Benedetti, …, G. Dietler. 2018. Identification and nanomechanical characterization of the fundamental single-strand protofilaments of amyloid α-synuclein fibrils. *Proc. Natl. Acad. Sci.* 115:7230–7235.

68. Kurouski, D., R. P. Van Duyne, and I. K. Lednev. 2015. Exploring the structure and formation mechanism of amyloid fibrils by Raman spectroscopy: a review. *Analyst.* 140:4967–4980.

69. Kurouski, D., T. Deckert-Gaudig, …, I. K. Lednev. 2014. Surface characterization of insulin protofilaments and fibril polymorphs using tip-enhanced Raman spectroscopy (TERS). *Biophys. J.* 106:263–271.

70. Li, B., P. Ge, …, L. Jiang. 2018. Cryo-EM of full-length α-synuclein reveals fibril polymorphs with a common structural kernel. *Nat. Commun.* 9:3609.

71. Guerrero-Ferreira, R., N. M. Taylor, …, H. Stahlberg. 2018. Cryo-EM structure of alpha-synuclein fibrils. *Elife.* 7:e36402.

72. Concha-Marambio, L., S. Pritzkow, …, C. Soto. 2023. Seed amplification assay for the detection of pathologic alpha-synuclein aggregates in cerebrospinal fluid. *Nat. Protoc.* 18:1179–1196.

73. Barth, A. 2007. Infrared spectroscopy of proteins. *Biochim. Biophys. Acta.* 1767:1073–1101.

74. Ruggeri, F. S., J. Habchi, …, T. P. J. Knowles. 2021. Infrared nanospectroscopy reveals the molecular interaction fingerprint of an aggregation inhibitor with single A β42 oligomers. *Nat. Commun.* 12:688.

75. Ruggeri, F. S., T. Šneideris, T. P. Knowles…, 2019. Characterizing individual protein aggregates by infrared nanospectroscopy and atomic force microscopy. *J. Vis. Exp.* 151:e60108.

76. Ruggeri, F. S., G. Longo, …, G. Dietler. 2015. Infrared nanospectroscopy characterization of oligomeric and fibrillar aggregates during amyloid formation. *Nat. Commun.* 6:7831.

77. Waeytens, J., J. Mathurin, …, A. Dazzi. 2021. Probing amyloid fibril secondary structures by infrared nanospectroscopy: experimental and theoretical considerations. *Analyst.* 146:132–145.

78. Iyer, A., S. J. Roeters, …, V. Subramaniam. 2017. C-terminal truncated α-synuclein fibrils contain strongly twisted β-sheets. *J. Am. Chem. Soc.* 139:15392–15400.

79. Hoyer, W., D. Cherny, …, T. M. Jovin. 2004. Impact of the acidic C-terminal region comprising amino acids 109- 140 on α-synuclein aggregation in vitro. *Biochemistry.* 43:16233–16242.

80. Serpell, L. C., J. Berriman, …, R. A. Crowther. 2000. Fiber diffraction of synthetic α-synuclein filaments shows amyloid-like cross-β conformation. *Proc. Natl. Acad. Sci.* 97:4897–4902.

81. Giliberti, V., R. Polito, …, M. Ortolani. 2019. Tip-enhanced infrared difference-nanospectroscopy of the proton pump activity of bacteriorhodopsin in single purple membrane patches. *Nano Lett.* 19:3104–3114.

82. Lu, F., M. Jin, and M. A. Belkin. 2014. Tip-enhanced infrared nanospectroscopy via molecular expansion force detection. *Nat. Photonics.* 8:307–312.

83. Temperini, M. E., R. Polito, …, V. Giliberti. 2024. An Infrared Nanospectroscopy Technique for the Study of Electric-Field-Induced Molecular Dynamics. *Nano Lett.* 24:9808–9815.

84. Karjalainen, E.-L., H. K. Ravi, and A. Barth. 2011. Simulation of the amide I absorption of stacked β-sheets. *J. Phys. Chem. B.* 115:749–757.

85. Schweitzer-Stenner, R. 2006. Advances in vibrational spectroscopy as a sensitive probe of peptide and protein structure: A critical review. *Vib. Spectrosc.* 42:98–117.

86. Knowles, T. P., A. W. Fitzpatrick, …, M. E. Welland. 2007. Role of intermolecular forces in defining material properties of protein nanofibrils. *Science.* 318:1900–1903.

87. Ruggeri, F. S., J. Adamcik, …, G. Dietler. 2015. Influence of the β--sheet content on the mechanical properties of aggregates during amyloid fibrillization. *Angew. Chem.* 127:2492–2496.

88. Ruggeri, F. S., T. Šneideris, …, T. P. J. Knowles. 2019. Atomic force microscopy for single molecule characterisation of protein aggregation. *Arch. Biochem. Biophys.* 664:134–148.

89. Yang, Y., Y. Shi, …, M. Goedert. 2022. Structures of α-synuclein filaments from human brains with Lewy pathology. *Nature*. 610:791–795.

90. Schweighauser, M., Y. Shi, …, M. Goedert. 2020. Structures of α--synuclein filaments from multiple system atrophy. *Nature.* 585:464–469.